

See discussions, stats, and author profiles for this publication at: <https://www.researchgate.net/publication/7464085>

# Dynamic Effects in MAS and MQMAS NMR Spectra of Half-Integer Quadrupolar Nuclei: Calculations and an Application to the Double Perovskite Cryolite

ARTICLE in JOURNAL OF THE AMERICAN CHEMICAL SOCIETY · DECEMBER 2005

Impact Factor: 12.11 · DOI: 10.1021/ja0549749 · Source: PubMed

---

CITATIONS

23

---

READS

19

## 4 AUTHORS, INCLUDING:



**Mrignayani Kotecha**

University of Illinois at Chicago

25 PUBLICATIONS 406 CITATIONS

SEE PROFILE



**Clare P Grey**

University of Cambridge

429 PUBLICATIONS 11,355 CITATIONS

SEE PROFILE



**Lucio Frydman**

Weizmann Institute of Science

220 PUBLICATIONS 6,117 CITATIONS

SEE PROFILE

## Dynamic Effects in MAS and MQMAS NMR Spectra of Half-Integer Quadrupolar Nuclei: Calculations and an Application to the Double Perovskite Cryolite

Mrignayani Kotecha,<sup>†</sup> Santanu Chaudhuri,<sup>‡</sup> Clare P. Grey,<sup>‡</sup> and Lucio Frydman<sup>\*,†</sup>

Contribution from the Department of Chemical Physics, Weizmann Institute of Science, 76100 Rehovot, Israel, and Department of Chemistry, State University of New York at Stony Brook, Stony Brook, New York 11794-3400

Received July 24, 2005; E-mail: lucio.frydman@weizmann.ac.il

**Abstract:** Dynamic processes such as chemical exchange or rotations between inequivalent orientations can affect the magic-angle spinning (MAS) and the multiple-quantum (MQ) MAS NMR spectra of half-integer quadrupolar nuclei. The present paper discusses such dynamic multisite MAS and MQMAS effects and applies them to study the dynamic processes that occur in the double perovskite cryolite, Na<sub>3</sub>AlF<sub>6</sub>. Dynamic line shape simulations invoking a second-order broadening of the central transition and relying on the semiclassical Bloch–McConnell formalism for chemical exchange were performed for a variety of exchange models possessing different symmetries. Fitting experimental variable-temperature cryolite <sup>23</sup>Na NMR data with this formalism revealed that the two inequivalent sodium sites in this mineral undergo an exchange characterized by a broad distribution of rates. To further assess this dynamic process a variety of <sup>27</sup>Al and <sup>19</sup>F MAS NMR studies were also undertaken; quantitative <sup>27</sup>Al–<sup>19</sup>F dipolar coupling measurements then revealed a dynamic motion of the AlF<sub>6</sub> octahedra that were qualitatively consistent with predictions stemming from molecular dynamic simulations on this double perovskite.

### 1. Introduction

Solid state NMR spectroscopy offers a variety of approaches for the characterization of nanoscale dynamics. As extensively discussed in the literature,<sup>1–6</sup> dynamic processes can modulate in different ways the isotropic and the anisotropic components of the NMR interactions, bringing about changes in the line shapes of NMR spectra and defining the nature of the nuclear spin relaxation processes. These effects can be monitored as a function of temperature and, if suitably analyzed, can then be interpreted in terms of models yielding insight into the nature of the dynamics. Nuclei with spin number  $I = 1$ , deuterium in particular, have long served as probes for studying dynamics in the solid phase thanks to the large quadrupolar anisotropies that characterize them.<sup>3–6</sup> Recent years have also witnessed a surging interest in solid-state dynamic NMR analyses based on the spectroscopy of half-integer quadrupolar nuclei possessing spin quantum numbers  $I \geq 3/2$ .<sup>7–11</sup> This in turn has been brought about by methodological advancements in spectral resolution

and in assignment techniques, which have enabled a wider use of this kind of nuclei in a variety of applications. High-field static experiments as well as magic-angle spinning (MAS) measurements carried out alone or in combination with multiple-quantum (MQMAS) and satellite-transition (STMAS) spectroscopies, have been particularly useful in advancing a variety of inorganic, bioinorganic, and material studies.<sup>12,13</sup> Most of these investigations have been of a structural nature, and relatively few have focused on the effects that dynamics may impose on the solid-state NMR line shapes of half-integer quadrupoles, particularly on central-transition second-order quadrupole patterns. Yet dynamic processes can also occur in a variety of solids, significantly affecting their properties. The purpose of the present paper is to discuss how molecular motions influence the NMR powder patterns arising from half-integer quadrupole nuclei in MAS and MQMAS experiments. This insight is then exploited to investigate the dynamics that occur in the double perovskite cryolite. Following a description of the structure and of some of the prior NMR

<sup>†</sup> Weizmann Institute of Science.

<sup>‡</sup> State University of New York at Stony Brook.

- (1) Spiess, H. W. *NMR: Basic Principles and Progress* **1978**, 15, 1.
- (2) Mehring, M. *High-Resolution NMR in Solids*; Springer-Verlag: Berlin, 1983.
- (3) Spiess, H. W. *Adv. Polym. Sci.* **1985**, 66, 23.
- (4) Schmidt-Rohr K.; Spiess, H. W. *Multidimensional Solid-State NMR and Polymers*; Academic Press: London, 1994.
- (5) Hoatson G. L.; Vold, R. L. *NMR: Basic Principles and Progress* **1994**, 32, 1.
- (6) Duer, M. J. Ed. *Solid State NMR: Theory and Applications*; Blackwell Science: London, 2001.

- (7) Witschas, M.; Eckert, H.; Freiheit, H.; Putnis, A.; Korus, G.; Jansen, M. *J. Phys. Chem. A* **2001**, 105, 6808.
- (8) Kristensen, J. H.; Farnan, I. *J. Chem. Phys.* **2001**, 114, 9608.
- (9) Schurko, R. W.; Wi, S.; Frydman, L. *J. Phys. Chem. A* **2002**, 106, 51.
- (10) Ashbrook, S.; Antonijevic, S.; Berry, A. J.; Wimperis, S. *Chem. Phys. Lett.* **2002**, 364, 634.
- (11) Larsen, F. H. *J. Magn. Reson.* **2004**, 171, 293.
- (12) Smith, M. E.; van Eck, E. R. H. *Prog. Nucl. Magn. Reson. Spectrosc.* **1999**, 34, 159.
- (13) Laws, D. D.; Bitter, H.-M. L.; Jerschow, A. *Angew. Chem., Int. Ed.* **2002**, 41, 3096.

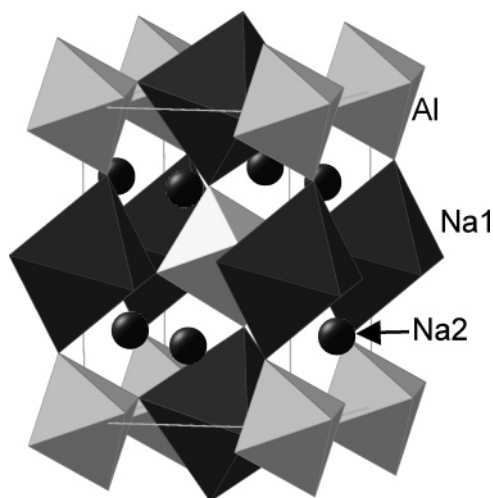


**Figure 1.** Structure of double perovskite cryolite, showing the corner connected  $\text{AlF}_6$  and  $\text{NaF}_6$  octahedra and the Na2 sites located between these octahedra.

work performed on cryolite and related systems, we present the relevant theory required to simulate the line shapes. These are then used to interpret the dynamic behavior revealed by this mineral.

A variety of interesting and technologically relevant materials are derived from the prototype  $\text{ABX}_3$  perovskite structure, including the copper-oxide based high-temperature superconductors and electroceramics.<sup>14,15</sup> The perovskite structure is made up of corner-sharing  $\text{BX}_6$  octahedra, the A site occupying the large eight-coordinated interstitial site between the connected octahedra. In double-perovskites ( $\text{A}_2\text{BB}'\text{X}_6$ ) such as cryolite,  $\text{Na}_2(\text{NaAl})\text{F}_6$ , the structure now comprises alternating corner-sharing  $\text{AlF}_6$  and  $\text{NaF}_6$  ( $\text{BX}_6$  and  $\text{B}'\text{X}_6$ ) octahedra, the A site being occupied by a second Na atom (Figure 1). The ratio between the multiplicities of the eight-coordinated Na2 and the octahedrally coordinated Na1 site is 2:1. The mismatch in the radius of the A-cation and the size of the hole formed by the corner sharing  $\text{BX}_6$  octahedra leads to octahedral tilting, with the  $\text{Al}-\text{F}-\text{Na1}$  bond angles dropping from an ideal value of  $180^\circ$  (in a cubic perovskite) to  $142\text{--}149^\circ$  in the room temperature cryolite phase.<sup>16,17</sup> This results in the A and B sites lowering their symmetries from cubic and octahedral to only an inversion symmetry, and a drop of the overall space group to  $P2_1/n$  (monoclinic). Single crystal and powder X-ray diffraction<sup>16,17</sup> as well as NMR studies<sup>18</sup> have investigated the potential atomic motions associated with phase transitions in cryolite. These earlier studies have shown that a fluctuation-induced first-order phase transition takes place at  $\sim 550^\circ\text{C}$  to form a high-temperature cubic phase. According to NMR this could arise from two coupled motions, involving a rotation of the nearly rigid  $\text{AlF}_6$  group, together with a displacement of the Na2 ion in the cavity from its equilibrium position.<sup>18,19</sup> Indeed, according to Spearing et al., cryolite at ambient temperature possesses no large amplitude motions.<sup>18</sup> But as the

temperature increases the rigid  $\text{AlF}_6$  units begin to oscillate, distorting the less rigid  $\text{NaF}_6$  octahedra, widening the space between the Na sites and allowing exchange to occur between the two Na sites. Ion motion has been detected by  $^{23}\text{Na}$  two-dimensional magnetization exchange methods at temperatures as low as  $150^\circ\text{C}$  by Lacassagne et al.; motions involving the  $\text{AlF}_6^{3-}$  ions were also observed by one-dimensional  $^{19}\text{F}$  and  $^{27}\text{Al}$  methods above  $150^\circ\text{C}$ .<sup>20</sup> This solid is thus an interesting one to study both in terms of its own structure and dynamics, and as a target for dynamic quadrupolar line shape analyses.

## 2. Theory

**Semiclassical Exchange Formalism Applied to MAS and MQMAS NMR.** We shall focus on solid-state NMR experiments with systems that are dominated by a variety of first- and second-order spin interactions. A number of approaches have been proposed to account for the effects that dynamics may introduce on these couplings, and on the resulting NMR spectra. For the purpose of this discussion we find it convenient to extend the semiclassical Bloch–McConnell formalism<sup>21,22</sup> recently employed to analyze central-transition dynamic  $I \geq 3/2$  line shapes,<sup>9</sup> to the instance of rotating solids. The relevant high-field Hamiltonian for the half integer quadrupolar nucleus was thus assumed<sup>23,24</sup>

$$H = H_Q^{(1)} + H_{CS}^{(1)} + H_Q^{(2)} \quad (1)$$

Here  $H_Q^{(1)}$  and  $H_Q^{(2)}$  are first- and second-order quadrupolar effects

$$H_Q^{(1)} = \frac{eQ}{2I(2I-1)\hbar} R_{20}^{(Q)} [3I_z^2 - I(I+1)] \quad (2a)$$

$$H_Q^{(2)} = \frac{3}{\omega_o} \left[ \frac{eQ}{2I(2I-1)\hbar} \right]^2 \{ R_{2-1}^{(Q)} R_{21}^{(Q)} I_z [4I(I+1) - 8I_z^2 - 1] + R_{2-2}^{(Q)} R_{22}^{(Q)} I_z [2I(I+1) - 2I_z^2 - 1] \} \quad (2b)$$

where  $eQ/[2I(2I-1)\hbar]$  and  $\{R_{2m}^{(Q)}\}_{m=0,\pm 1,\pm 2}$  define the strength and the orientation dependence of the quadrupole interaction.  $H_{CS}^{(1)}$  in eq 1 is the usual chemical shift interaction Hamiltonian given to first-order by

$$H_{CS}^{(1)} = \left[ \sigma_{iso} \omega_0 + \frac{2}{\sqrt{6}} R_{20}^{(CS)} B_0 \right] I_z \quad (3)$$

with  $\sigma_{iso}$  as the isotropic chemical shielding and  $R_{20}^{(CS)}$  as the shielding anisotropy. These expressions can be used to calculate arbitrary rotating frame frequencies within the quadrupolar manifold; in particular the central ( $-1/2 \leftrightarrow +1/2$ ) and the triple-

(14) v. Naray-Szabo, St.; Sasvari, K. Z. *Kristallogr.* **1938**, 99, 27.

(15) Suzuki, K. *J. Phys. Soc. Jpn.* **1995**, 64, 674.

(16) Yang, H.; Ghose, S.; Hatch, D. *Phys. Chem. Miner.* **1993**, 19, 528.

(17) Zhou, Q.; Kennedy, B. J. *J. Solid State Chem.* **2004**, 177, 654.

(18) Spearing, D. R.; Stebbins J. F.; Farnan, I. *Phys. Chem. Miner.* **1994**, 21, 373.

(19) Du, L. S. Ph.D. Thesis, SUNY Stony Brook, Chapter 4, 2000.

(20) Lacassagne, V.; Bessada, C.; Massiot, D.; Florian, P.; Coutures, J. P. *J. Chim. Phys.* **1998**, 95, 322.

(21) McConnell, H. M. *J. Chem. Phys.* **1958**, 28, 430.

(22) Abragam, A. *Principles of Nuclear Magnetism*; Oxford University Press: New York, 1961.

(23) Freude, D.; Haase, J. *NMR: Basic Principles and Progress* **1993**, 29, 1.

(24) Frydman, L. *Annu. Rev. Phys. Chem.* **2001**, 52, 463.

quantum ( $-3/2 \leftrightarrow +3/2$ ) transitions evolution frequencies become

$$\omega_{1/2 \leftrightarrow -1/2} = \sigma_{iso} \omega_o + \frac{2}{\sqrt{6}} B_o R_{20}^{(CS)} + \frac{3}{2\omega_o} \left( \frac{eQ}{2I(2I-1)\hbar} \right)^2 [4I(I+1) - 3][2R_{2-1}^{(Q)} R_{21}^{(Q)} + R_{2-2}^{(Q)} R_{22}^{(Q)}] \quad (4)$$

and

$$\omega_{3/2 \leftrightarrow -3/2} = 3\sigma_{iso} \omega_o + \sqrt{6} B_o R_{20}^{(CS)} + \frac{9}{\omega_o} \left( \frac{eQ}{2I(2I-1)\hbar} \right)^2 \{ [4I(I+1) - 19] R_{2-1}^{(Q)} R_{21}^{(Q)} + [2I(I+1) - 11/2] R_{2-2}^{(Q)} R_{22}^{(Q)} \} \quad (5)$$

Equations 4 and 5 can be used to account for the effects of chemical exchange or motions on MAS and MQMAS NMR spectra, provided that their spatial components are expressed in some intermediate molecular or lattice frame (MOL) that is common for all interconverting sites. Transforming the various tensorial components from their principal axis systems (PASs), via this MOL intermediate frame and onward to the laboratory (LAB) frame, can be carried out with the help of second-rank Wigner rotation matrices<sup>25</sup> defined by Euler angles.

$$\begin{array}{ccc} \rho_{2\pi m}^{(CS)}(\alpha', \beta', \gamma') & \xrightarrow{(\varphi, \theta, \phi)} & R_{2\pi m}^{(\lambda)}(MOL) \\ \rho_{2\pi m}^{(Q)}(\alpha, \beta, \gamma) & \xrightarrow{(-\omega_r t, \theta_m, 0)} & R_{2\pi m}^{(\lambda)}(ROT) \end{array} \quad \begin{array}{c} \longrightarrow \\ \longrightarrow \end{array} \quad R_{2\pi m}^{(\lambda)}(LAB) \quad (6)$$

Here  $(\varphi, \theta, \phi)$  denotes a set of powder angles to be suitably integrated over the solid sphere in order to describe all possible orientations of the intermediate MOL frame with respect to the spinning rotor (ROT), that is itself related to the LAB frame through a  $(-\omega_r t, \theta_m, 0)$  transformation defined by the spinning frequency  $\omega_r$  and the magic angle  $\theta_m$ . In the current study such transformations were implemented numerically to calculate the time-dependent evolution frequencies from the various exchanging sites, located in different crystallites.

A stochastic dynamics between different exchanging sites will change the local evolution frequencies experienced by the spins at each orientation, bringing about significant changes in the appearance of the powder-averaged MAS and MQMAS spectra. To account for this process we relied on a simplified description arising from McConnell's semiclassical treatment of exchange, which modifies the Bloch equations describing the time dependence of a magnetization vector  $\mathbf{M}(t)$  possessing  $N$  elements  $M_j(t)$  corresponding to each of the exchanging sites, according to<sup>1-6</sup>

$$\frac{d\mathbf{M}}{dt} = [i\bar{\omega}(t) + \bar{\Pi}] \cdot \mathbf{M}(t) \quad (7)$$

where  $\bar{\omega}$  is an  $N \times N$  diagonal matrix comprised by the time-dependent MAS precession frequencies of the various exchange-

ing sites, including for the case of MQMAS experiments the central- (1Q) and triple-quantum (3Q) transitions, and  $\bar{\Pi}$  is an  $N \times N$  matrix characterizing the Markovian exchange process according to its topology and to its transition rates. The total magnetization  $\mathbf{M}(t)$  can then be used to compute the free induction decay (FID) measured experimentally, proportional to the total magnetization  $G(t) = \sum_{j=1}^N M_j(t) = \bar{\mathbf{1}} \cdot \mathbf{M}(t)$ . In the case of static solids, where the sites' evolution frequencies are constant, this FID function can then be formally expressed as

$$G(t) = \mathbf{1} \cdot e^{[i\bar{\omega} + \bar{\Pi}]t} \cdot \mathbf{W} \quad (8)$$

with  $\mathbf{W}$  being a column vector representing the relative populations of each site. For MAS and MQMAS experiments however the evolution frequencies  $\bar{\omega}(t)$  are rendered time-dependent due to the sample spinning, and an analytical integration of eq 8's exponent becomes unavailable. FIDs in these cases were therefore computed by partitioning each rotor period  $T_r = 2\pi/\omega_r$  within the evolution/acquisition times into  $M$  intervals  $\Delta t \ll T_r$ , calculating a corresponding set of discrete time propagators for the spins' magnetizations  $U(t_i) \approx \exp\{[i\bar{\omega}(t_i) + \bar{\Pi}] \cdot \Delta t\}$ , and using the resulting propagators to derive the time-domain signal as

$$\begin{aligned} G_{MAS}(t = M\Delta t) &= \mathbf{1} \cdot \left[ \prod_{i=1}^M U(t_i) \right] \cdot \mathbf{W} \\ G_{MQMAS}(t_1 = M_1\Delta t, t_2 = M_2\Delta t) &= \mathbf{1} \cdot \left[ \prod_{j=1}^{M_1} U_{3Q}(t_j) \right] \left[ \prod_{k=1}^{M_2} U_{1Q}(t_k) \right] \cdot \mathbf{W} \quad (9) \end{aligned}$$

for the MAS and MQMAS experiments, respectively. In the present study the calculation of the piecewise-constant  $U(t_i)$  propagator was carried out by diagonalizing the non-Hermitian evolution matrix  $i\bar{\omega}(t_i) + \bar{\Pi}$  for every crystallite orientation in the powder; signals were then powder-integrated over all  $(\varphi, \theta, \phi)$  Euler angles. Notice that due to their simplified nature, such simulations paid no attention to the excitation or conversion details of the 3Q coherence in the MQMAS experiments.<sup>26,27</sup> Furthermore, and as described elsewhere in more detail,<sup>9</sup> this formalism cannot cope with the complete range of dynamic quadrupole-driven changes. Still, it offers a simple route to describing spectral effects when exchange rates are on the order of the second-order quadrupole couplings, and is thus useful on a wide range of scenarios including those found in cryolite.

**Examples of Static, MAS, and MQMAS Dynamic NMR Spectra.** Equipped with the numerical formalism just described for analyzing multisite exchange in half-integer quadrupolar nuclei, we considered it worthwhile to examine some basic line shape features introduced by dynamics. We begin by comparing in Figure 2 the variations that static and MAS line shapes dominated by first-order shielding vis-à-vis second-order quadrupolar interactions will display, for two sites undergoing a jump process between equally populated but orthogonal

(25) Haeberlen, U. *Advances in Magnetic Resonance, Supplement I*; Waugh, J. S., Ed.; Academic Press: New York, 1976.

(26) Marinelli, L.; Frydman, L. *Chem. Phys. Lett.* **1997**, 275, 188.

(27) Friedrich, U.; Schnell, I.; Brown, S. P.; Lupulescu, A.; Demco, D. E.; Spiess, H. W. *Mol. Phys.* **1998**, 95, 1209.

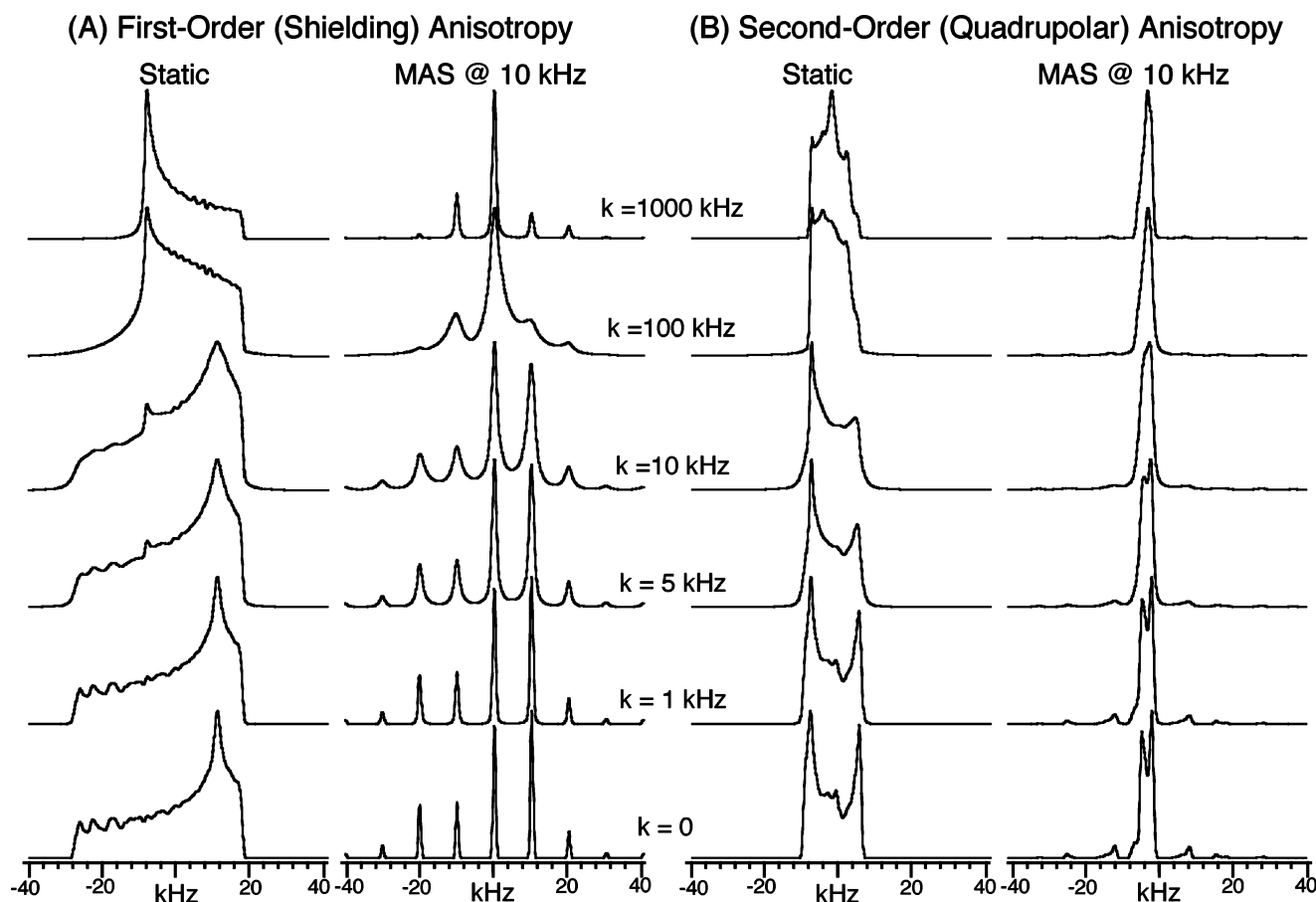


**Figure 2.** Comparison between the dynamic effects introduced by a two-site exchange process on the static and the MAS NMR spectra of (A) a central transition line shape affected solely by first-order shielding anisotropy and (B) a central transition line shape affected solely by second-order quadrupole effects. In all cases spectra were computed for equal populations and different exchange rates  $k$  and convoluted with an 800 Hz wide Lorentzian line shape before presentation. The following parameters were assumed in the simulations:  $I = 5/2$ ,  $\omega_0/2\pi = 85.7$  MHz,  $\omega_r/2\pi = 10$  kHz (for MAS),  $\delta_{\text{iso}} = 0$  ppm, Euler angles  $\alpha_1 = \beta_1 = \gamma_1 = \alpha_2 = \gamma_2 = 0$ ,  $\beta_2 = 90$ . In addition  $\delta_{\text{CS}} = -324$  ppm,  $\eta_{\text{CS}} = 0.24$  for (A);  $e^2qQ/h = 6.3$  MHz,  $\eta_Q = 0.1$  for (B). As throughout the rest of this work the electric field gradient tensor principal components were defined as  $|V_{yy}| \leq |V_{xx}| \leq |V_{zz}|$  with  $\eta_Q = (V_{yy} - V_{xx})/V_{zz}$ ; anisotropic chemical shifts were described according to  $|\delta_{yy}| \leq |\delta_{xx}| \leq |\delta_{zz}|$ ,  $\delta_{\text{CS}} = \delta_{zz}$ , and  $\eta_{\text{CS}} = (\delta_{yy} - \delta_{xx})/\delta_{zz}$ .

orientations, as a function of the jump rate  $k$ . Shown on the left-hand panels is the behavior displayed by sites dominated by shielding anisotropy, and on the right-hand is that displayed by comparable second-order effects. The nonspinning spectra are characterized by differing line shapes due to the different spatial ranks involved in the first- and second-order effects.<sup>9</sup> Even further differences arise when comparing the corresponding dynamic MAS line shapes: the second-order patterns exhibit only moderate dynamic changes, while the first-order ones display significant broadenings in the center- and sideband peaks and a concomitant drop in absolute signal intensity. This decrease in the maximum heights of the frequency-domain peaks has been described in the literature and is known to arise from the destructive interference that dynamics exert on the MAS averaging of shielding anisotropies.<sup>28,29</sup> By contrast there is little that MAS can interfere with in the second-order quadrupolar case, where under normal conditions line shapes are dominated by time-independent fourth-rank residual anisotropies. Consequently the differences with the static case are in this instance minor, noticeable mostly as a slight broadening in the spinning sidebands, and by a lengthening of the relevant NMR time scale (decrease in the relevant exchange rates) due to the MAS-driven

scaling of the anisotropy. Similar simulations were repeated for a variety of different exchange processes involving two-, three-, and four-site jumps, as well as for quadrupolar asymmetry parameters ranging from zero to one. In all cases the line shapes showed a behavior that is qualitatively similar to that illustrated on the right-hand side of Figure 2.

In some respects MQMAS can be considered to do for the sake of averaging away the anisotropies of half-integer quadrupolar nuclei, what MAS does on behalf of dilute spin  $1/2$ . Given the significant interfering effects that dynamics has in the latter shielding scenario, strong dynamic effects can also be expected to arise in the MQMAS spectroscopy of exchanging quadrupoles. Figure 3 considers with numerical simulations such a dynamic MQMAS case, presenting the expectations arising from two exchanging sites which have identical quadrupole coupling parameters but tensorial PASs related by a  $90^\circ$  rotation along their main  $V_{zz}$  axes. It is clear by comparing this figure with its analogous static and MAS cases that exchange does indeed affect significantly the width (and the intensity) of the MQMAS spectral peaks. As in the spin  $1/2$  dynamic MAS case this stems from the fact that MQMAS is based on a staged refocusing of the anisotropic dephasing, and any dynamic process that changes the precession frequencies at a microscopic level will therefore interfere with its coherent echo formation.

(28) Maricq, M. M.; Waugh, J. S. *J. Chem. Phys.* **1979**, *70*, 3300.

(29) Schmidt, A.; Vega, S. *J. Chem. Phys.* **1987**, *87*, 6895.



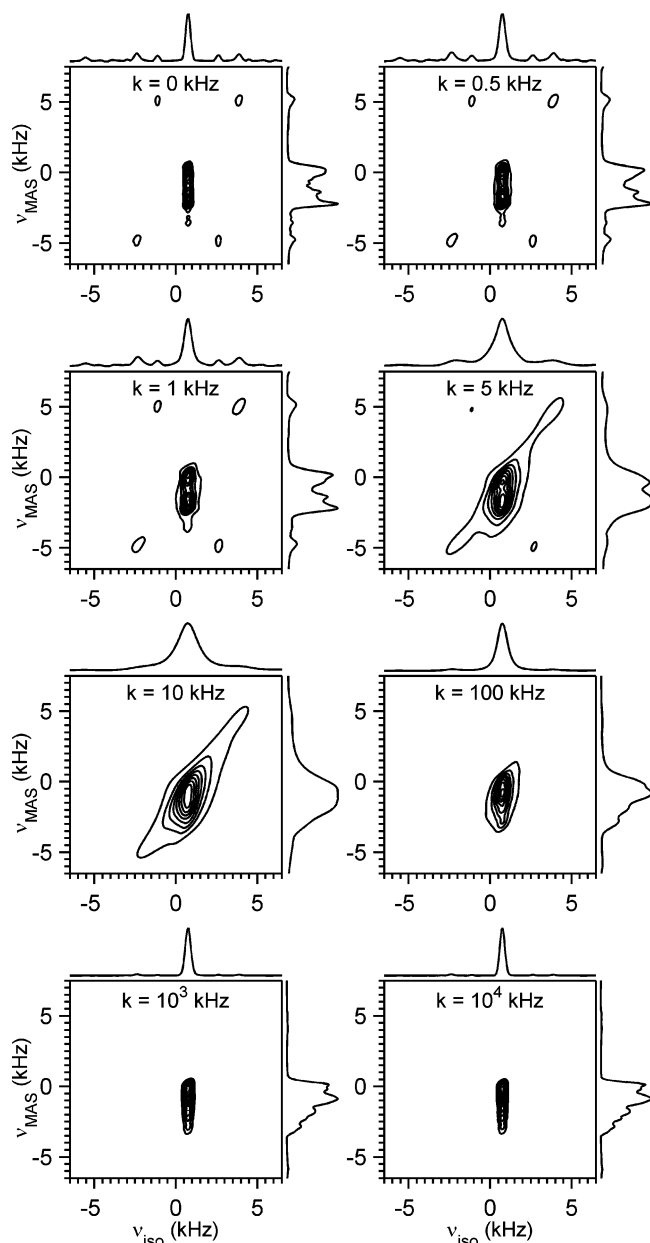


**Figure 3.** Effects introduced by dynamics on the 2D MQMAS powder NMR spectrum of a quadrupolar nucleus undergoing a two-site exchange between different orientations, as a function of the exchange rate  $k$ . The 2D spectrum shows purely absorptive line shapes as a result of a hypercomplex combination of 3Q/1Q evolutions<sup>30</sup> and has been sheared so as to reflect a purely isotropic spectrum along the horizontal and a MAS-like spectrum along the vertical dimensions. Simulation parameters included  $I = 5/2$ ,  $\omega_0/2\pi = 85.7$  MHz,  $\omega_r/2\pi = 5$  kHz,  $\delta_{\text{iso}} = \delta_{\text{CS}} = \eta_{\text{CS}} = 0$ , Euler angles  $\alpha_1 = \beta_1 = \gamma_1 = \alpha_2 = \gamma_2 = 0^\circ$ ,  $\beta_2 = 90^\circ$ ,  $e^2qQ/h = 4.5$  MHz,  $\eta_Q = 0.1$ , and an 800 Hz Lorentzian line broadening.

Figure 4 illustrates another case of interference between dynamics and MQMAS, this time involving a change in the chemical environments of the sites. As expected, also in this case the line shape effects introduced by the dynamics are significant; particularly along the indirect isotropic domain.

Unlike the case of chemical exchange in isotropic phases, the line shape changes depicted in Figures 2–4 will usually depend on multiple parameters besides the kinetic rate. These will include the exchange geometry, the sample spinning rate, and the strengths of the quadrupole and shielding anisotropies, etc. Furthermore crystallites in a powdered sample are expected

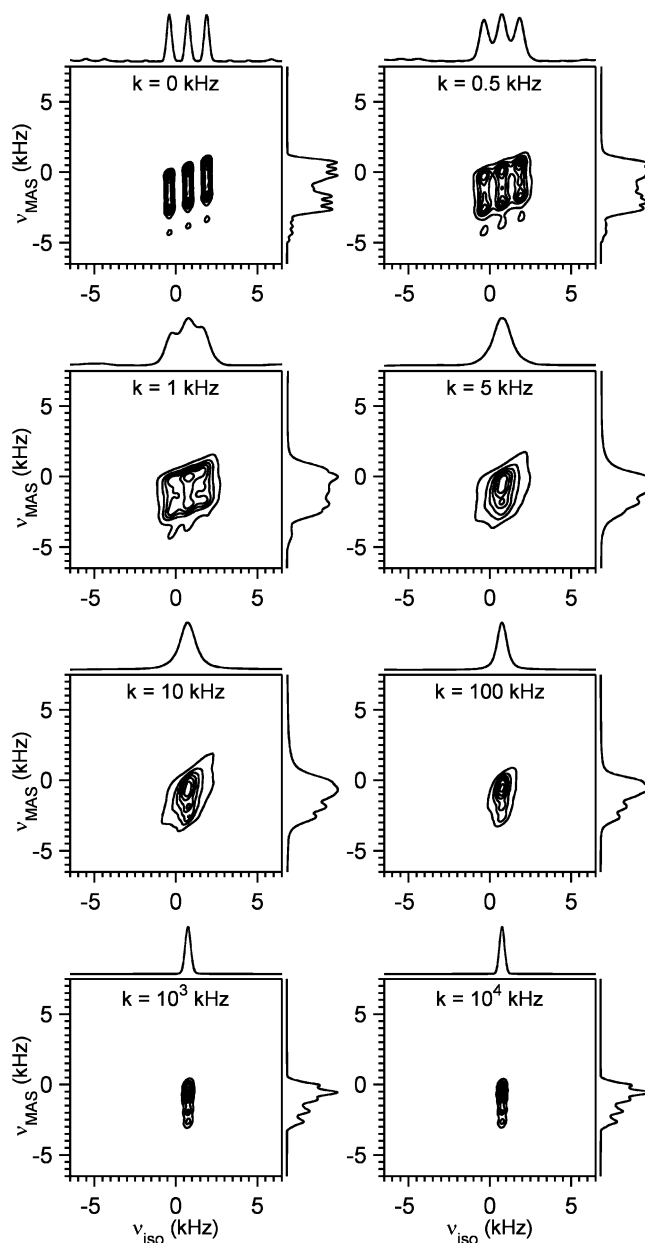


**Figure 4.** Idem as in Figure 3 ( $I = 5/2$ ,  $\omega_0/2\pi = 85.7$  MHz,  $\omega_r/2\pi = 10$  kHz) but for the case of exchange among three inequivalent chemical sites possessing common parameters  $e^2qQ/h = 4.5$  MHz,  $\eta_Q = 0.1$ ; and different parameters  $\delta_{\text{iso}1} = 10$  ppm,  $\delta_{\text{iso}2} = 0$  ppm,  $\delta_{\text{iso}3} = -10$  ppm,  $(\alpha, \beta, \gamma)_1 = (0^\circ, 125.3^\circ, 0^\circ)$ ,  $(\alpha, \beta, \gamma)_2 = (0^\circ, 125.3^\circ, 120^\circ)$ ,  $(\alpha, \beta, \gamma)_3 = (0^\circ, 125.3^\circ, 240^\circ)$  (Euler angles corresponding to an exchange about the  $C_3$  axis of a tetrahedron).

to display an array of dynamic time scales, leading in the intermediate exchange regime to complex overall line shapes. Still, in the search for a single characteristic capable of summarizing these various changes, we decided to focus on the maximal MAS and MQMAS peak intensities, which we expect to decrease as the exchange rate hits the intermediate regime and then return toward its initial value as the process becomes fast in the relevant time scale. Figure 5 summarizes for these two experiments a series of results deriving from numerical calculations on a  $90^\circ$  jump exchange model, which validate these “V”-shaped maximum-intensity vs rate expectations. These results also confirm that, due to its intrinsic echoing nature, 2D MQMAS line shapes will have their signals more significantly

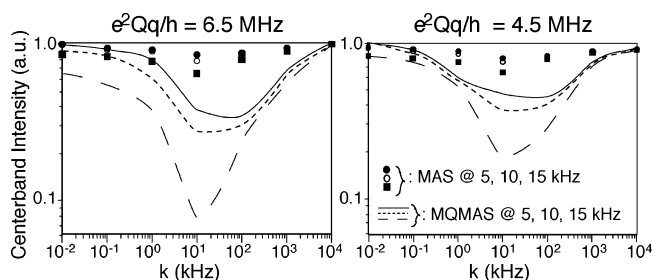


**Figure 5.** Log-log plots describing the intensity variations expected for the center peak of an exchanging site undergoing jumps at a rate  $k$  about two orthogonal orientations, when subject to MAS and MQMAS experiments. The variations arise from simulations under the following conditions:  $I = 5/2$ ,  $\omega_0/2\pi = 85.7$  MHz,  $\alpha_1 = \beta_1 = \gamma_1 = \alpha_2 = \gamma_2 = 0^\circ$ ,  $\beta_2 = 90^\circ$ , the indicated  $e^2qQ/h$  values with  $\eta_Q = 0.1$ , and spinning rates  $\omega_r/2\pi = 5$  kHz (●, —), 10 kHz (○, ---), 15 kHz (■, - - -).

affected than their 1D MAS counterparts, implying that the 2D method is capable of providing both higher spectral resolution as well as further dynamic insight than the simpler 1D alternative.

### 3. Materials and Methods

To explore some of the predictions made in the preceding section, a series of solid state NMR experiments were carried out on a cryolite obtained from Aldrich Chemicals. While not in the spectrometer this sample was mostly kept inside a desiccator to minimize possible changes arising from sample hydration; during the NMR studies humidity was avoided by flowing past the sample a thermostated  $N_2$  stream. All the  $^{23}\text{Na}$  NMR spectra presented in this work were recorded on a laboratory-built spectrometer operating at 7.2 T ( $^{23}\text{Na}$  frequency = 79.88 MHz) utilizing a commercial Varian/CMX 4 mm probehead capable of spinning samples up to 18 kHz, and a variable-temperature accessory capable of heating samples up to 250 °C.  $^{27}\text{Al}$  MAS NMR were also recorded on this sample; toward this end a laboratory-built spectrometer operating at 4.7 T ( $^{27}\text{Al}$  frequency = 52.37 MHz) and a 4 mm Varian/CMX probe were used. To obtain the 2D MQMAS and 2D exchange sodium data, phase-sensitive acquisitions with sign discrimination along both spectral dimensions were recorded.<sup>30</sup> The first of these experiments was collected using fast-amplitude modulation for enhancing the  $3Q \rightarrow 1Q$  transfer;<sup>31</sup> the latter relied on the traditional three-pulse sequence. In all experiments radio frequency fields in excess of 100 kHz were used for spin excitation; no need for  $^{19}\text{F}$  decoupling was noticed in these fast-spinning quadrupolar acquisitions.  $^{19}\text{F}$  MAS NMR experiments were also performed, on a CMX-II 360 MHz spectrometer at an operating frequency of 338.75 MHz with a 4 mm probehead. These spectra were externally referenced to  $\text{CFCl}_3$  at 0 ppm.

All dynamic spectra were simulated on an iMac G3 computer using custom-written c++ programs. The hemispherical step method was used for powder averaging,<sup>32</sup> and matrix diagonalization and inversion routines were performed using the LAPACK linear algebra package. For the calculation of distributed MAS spectra (vide infra) 10 to 12 points in log-Gaussian  $k$ -distribution curves were taken and their resulting subspectra were added up. For the  $^{27}\text{Al}$  NMR data, experiments were fitted with simulations arising from SIMPSON calculations<sup>33</sup> based on the actual acquisition conditions. Libration angle calculations were then done on the basis of these results using a custom-written MATLAB program.

(30) Ernst, R. R.; Bodenhausen, G.; Wokaun, A. *Principles of Nuclear Magnetic Resonance in One and Two Dimensions*; Clarendon: Oxford, 1987.

(31) Madhu, P. K.; Goldbourt, A.; Frydman, L.; Vega, S. *Chem. Phys. Lett.* **1999**, 307, 741.

(32) Edén, M.; Levitt, M. H. *J. Magn. Reson.* **1998**, 132, 200.

(33) Bak, M.; Rasmussen, J. M.; Nielsen, N. C. *J. Magn. Reson.* **2000**, 147, 296.

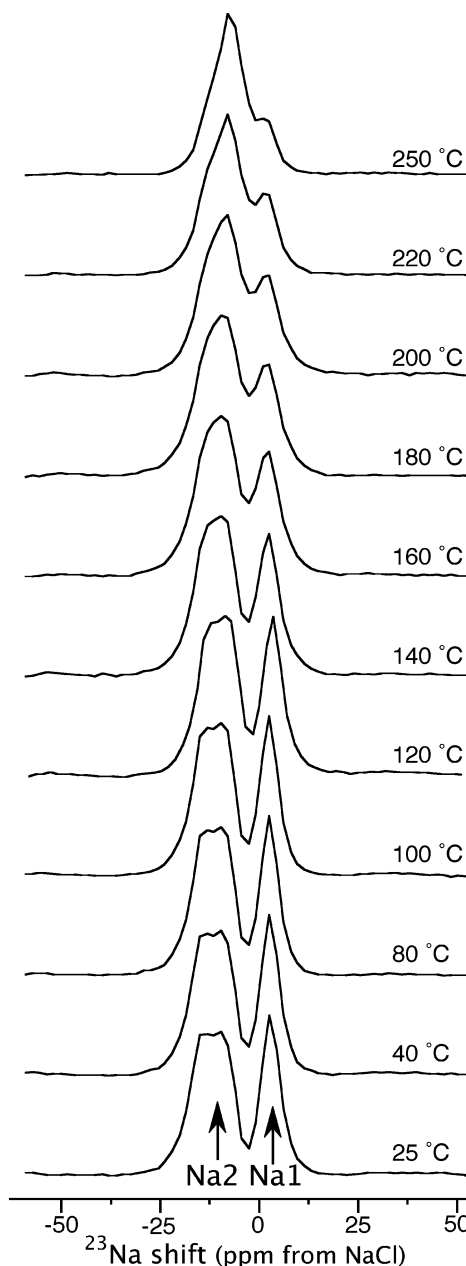


**Figure 6.**  $^{23}\text{Na}$  MAS NMR spectra of cryolite,  $\text{Na}_3\text{AlF}_6$ , recorded as a function of temperature. Data were recorded at 7.2 T (79.88 MHz Larmor frequency) at a spinning speed of 8 kHz, collecting 128 scans with a 6 s recycling delay.

### 4. Results

**Dynamic  $^{23}\text{Na}$  NMR of Cryolite:** As an application of the behavior described in the preceding section, we turn our focus to the dynamic effects arising in the solid state NMR spectra of cryolite,  $\text{Na}_3\text{AlF}_6$ . The  $^{23}\text{Na}$  MAS NMR spectra of this material contain two resolved resonances at room temperature (Figure 6) centered at approximately 4 and -8 ppm. These are assigned to the Na1 (octahedral) and Na2 (eight-coordinate) sites, respectively. The larger chemical shift for the Na1 site is consistent with its smaller coordination number. The Na2 eight-coordinate site has a larger  $e^2qQ/h$  value than that of the Na1 site (1.45 vs 0.9 MHz). These values were determined by simulation of the MAS and MQMAS data (see below) and are similar to those in a recent literature report (1.43 and 0.84 MHz

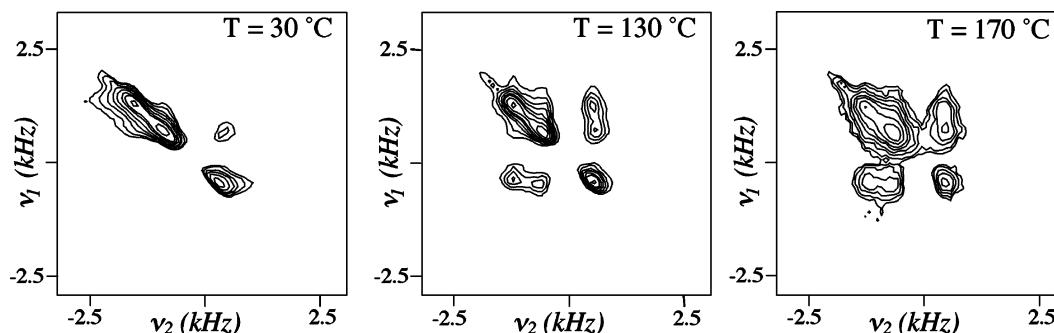


**Figure 7.**  $^{23}\text{Na}$  2D exchange MAS NMR spectra of cryolite, recorded at the indicated temperatures. All spectra were acquired using 15 kHz MAS, a 40 ms exchange time, and a purely absorptive echo/antiecho acquisition scheme based on phase cycling of the three-pulse sequence. The acquisitions involved 128 scans per  $t_1$  point and a 3 s recycle delay.

for Na2 and Na1<sup>34</sup>); they are also consistent with the large octahedral tilts of the corner sharing  $\text{BF}_6$  units seen at room temperature, resulting in a distorted environment for the Na2 atoms. The resonances slowly merge into one peak as temperature increases, consistent with the previous work of Spearing et al.<sup>18</sup> This behavior is typical of sites that undergo an exchange process at rates within the relevant NMR time scale. However, even at the highest temperature a weak Na1 resonance is still observed, suggesting a distribution of correlation times. Cryolite's putative motions are explored in more detail by the set of variable-temperature 2D exchange  $^{23}\text{Na}$  MAS NMR spectra shown in Figure 7, which probe motion in a time scale governed by the mixing time of the experiment. When considered in unison with the data shown in Figure 6, the existence of a thermally activated interchange among the two Na environments, at rates that at 150 °C are on the order of 0.1–1 kHz, becomes substantiated.

To obtain further insight into the rates of these dynamics, the  $^{23}\text{Na}$  1D MAS spectra recorded at 15 kHz as a function of temperature were simulated using the approach described in section 2. Figure 8 shows our best fit to the experimental spectra. These line shapes could not be reproduced with a simple model involving a single pair of forward/backward exchange rates. Instead a broad distribution of exchange rates had to be assumed, something that in turn hints to the presence of a distribution in the activation energies that define the dynamic process and/or a distribution in the number of defects across the solid. Specifically, for the simulations shown in Figure 8, a log-Gaussian distribution of the exchange rate  $k$  according to<sup>4</sup>

$$P(\ln k) = \frac{1}{\sigma\sqrt{2\pi}} \exp\left[-\frac{(\ln k/k_0)^2}{2\sigma^2}\right] \quad (10)$$

was used, where  $k_0$  defines the logarithmic mean value of the exchange rate while  $\sigma$  controls the width of the distribution. The effect of the various parameters on generic dynamic quadrupole MAS line shapes were extensively explored; in connection to the specific  $^{23}\text{Na}$  NMR data recorded for cryolite, simulations revealed that an increase in temperature resulted in only modest increases in the mean  $k_0$  rate but caused a large, sudden increase in the  $\sigma$  value at about 120 °C.

As a complement to this MAS NMR analysis, Figure 9 shows representative variable temperature MQMAS spectra of cryolite. The two different Na resonances are clearly resolved in the room

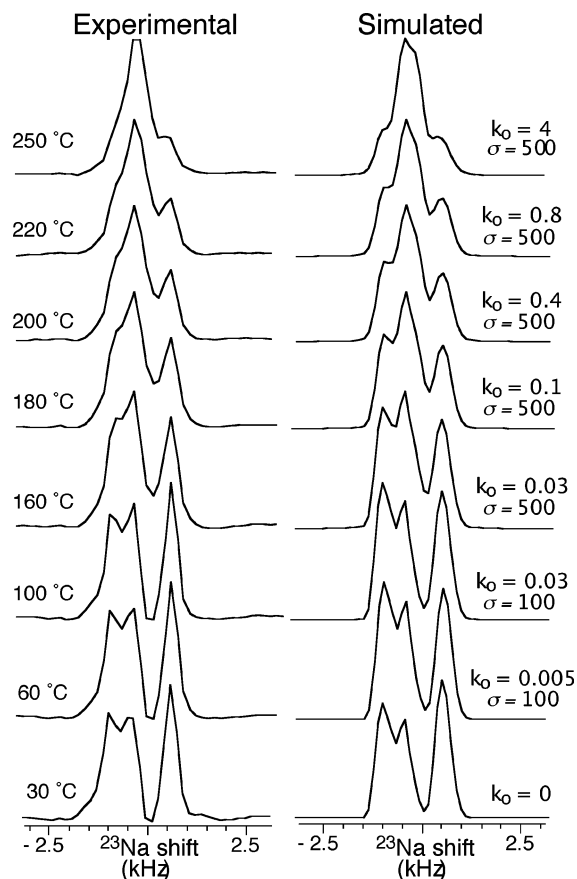


**Figure 8.** Comparison between the experimental temperature behavior observed in the  $^{23}\text{Na}$  MAS NMR spectrum of cryolite, and best-fit simulations calculated using the kinetic formalism described in the text. These simulations were obtained by varying the mean exchange rate  $k_0$  and the distribution in rates  $\sigma$  (eq 10; all in kHz) until observing an optimum match. Other parameters involved in these simulations were  $I = 3/2$ ,  $\omega_Q/2\pi = 79.88$  MHz,  $\omega_r/2\pi = 15$  kHz,  $(e^2qQ/h)_1 = 1.45$  MHz,  $(e^2qQ/h)_2 = 0.95$  MHz,  $\eta_{Q1} = 0.25$ ,  $\eta_{Q2} = 0.5$ ,  $\delta_{\text{iso}1} = -18$  ppm,  $\delta_{\text{iso}2} = 2.5$  ppm,  $\text{population}_1 = 2 \cdot \text{population}_2$ ,  $(\alpha, \beta, \gamma)_1 = (0, 60^\circ, 0)$  and  $(\alpha, \beta, \gamma)_2 = (0, 60^\circ, 180^\circ)$ . The listed coupling parameters were obtained from MQMAS data, whereas the relative tensor orientations gave the best-fitted line shapes.

temperature  $^{23}\text{Na}$  MQMAS spectrum, and no changes in the spectral appearance were observed upon reducing temperature all the way to  $-80$  °C. By contrast at higher temperatures, and with the onset of the exchange process, a substantial broadening begins to affect the high-resolution isotropic dimension. Yet as was the case for the MAS data, the MQMAS experiments reflect a distribution of exchange rates by their lack of a well-defined temperature at which the two isotropically resolved line shapes

(34) Silly, G.; Legein, C.; Buzare, J. Y.; Calvayrac, F. *Solid State NMR* **2004**, 25, 241.



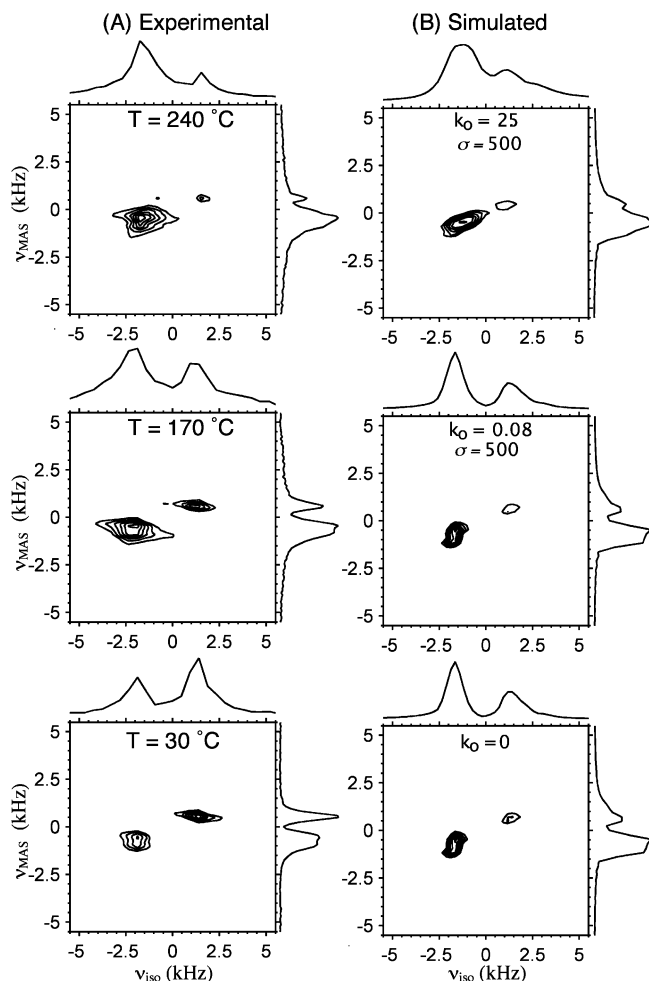


**Figure 9.** Comparison between (A) the variations exhibited by the  $^{23}\text{Na}$  2D MQMAS NMR spectra of cryolite as a function of temperatures: and (B) best fit 2D spectral simulations calculated using the theoretical formalism described in the text and the kinetic distribution parameters listed. All spectra were acquired while spinning at 15 kHz, sheared into an isotropic/anisotropic (MAS) representation, and displayed at identical contour levels against the normalized maximum intensity. The 2D simulations assumed the same quadrupole and isotropic shift parameters as those in Figure 8 and involved propagating spins along both MQMAS time domains over  $256 \times 256$  points separated by  $8.33 \mu\text{s}$  dwells under the conditions introduced in section 2, a Lorentz-Gauss weighting, and suitable Fourier/shearing transformations. 2D line shapes arising from 10  $k$ -points of the kinetic distribution function in eq 10 and the stated parameters (in kHz) were coadded to obtain these simulations.

collapse. A distribution of kinetic rates therefore had to be invoked in order to suitably reproduce the experimental 2D MQMAS NMR data sets; the parameters of such distribution ended up being remarkably similar to the ones arising from the 1D MAS NMR simulations.

**$^{27}\text{Al}$  and  $^{19}\text{F}$  Dynamic MAS NMR Behavior:** To gain further insight concerning the relationship between the  $^{23}\text{Na}$  NMR behavior and motions in cryolite, the thermal libration of  $\text{AlF}_6$  octahedra was explored using  $^{27}\text{Al}$  and  $^{19}\text{F}$  solid state MAS NMR. At ambient temperature the  $^{19}\text{F}$ -decoupled  $^{29}\text{Al}$  MAS NMR spectrum of cryolite shows a single chemical site, with a weak quadrupolar coupling constant  $e^2qQ/h$  of  $\sim 1$  MHz (Figure 10). This value is within the very wide range of values that have been reported in the literature, of between 0.6 and 2 MHz.<sup>18,20,34,35</sup> The satellite-transition spinning sideband pattern observed for this site decreases somewhat in intensity as temperature increases, consistent with an increased motion of

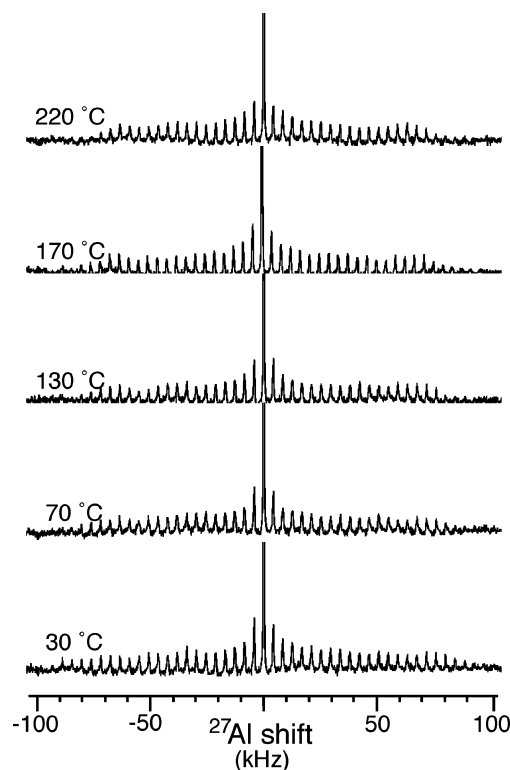


**Figure 10.** Temperature-dependent  $^{27}\text{Al}$  NMR spectra of cryolite recorded at 4 kHz MAS illustrating a gradual, minor averaging of the satellite transitions' sidebands.

the  $\text{AlF}_6$  units. These results suggest that the different dynamics of the  $\text{AlF}_6$  groups may be responsible for the very different values of  $e^2qQ/h$  and asymmetry parameters measured by different co-workers for materials with the same nominal composition.

$^{19}\text{F}$  MAS NMR spectra were also acquired for the perovskite as a function of temperature (Figure 11). The chemical shift moves gradually to lower frequency as the temperature is raised, with the intensity of the spinning sidebands gradually decreasing. Above  $125^\circ\text{C}$  the line width increases before decreasing again above  $200^\circ\text{C}$ , where a Lorentzian line shape is now observed. The smaller resonance at approximately  $-210$  ppm is ascribed to  $\text{NaF}$ , present as an impurity phase. The spectra are consistent with motion of the  $\text{AlF}_6$  units and with a reduction of the  $^{19}\text{F}$  homonuclear and of the  $^{27}\text{Al}$ – $^{19}\text{F}$  and  $^{23}\text{Na}$ – $^{19}\text{F}$  heteronuclear dipolar couplings. The transient line width increase of the  $^{19}\text{F}$  resonance as temperature increases is likely associated with an inference between a motional process and the MAS-driven averaging of the anisotropic interactions. As mentioned this effect is largest when the rate of the motion is comparable to the sample spinning rate and to the strength of the spin anisotropies,<sup>28,36</sup> which in this instance probably combine the  $^{19}\text{F}$  shift anisotropy together with  $^{27}\text{Al}$ – $^{19}\text{F}$ / $^{19}\text{F}$ – $^{19}\text{F}$  dipolar couplings. Line broadening due to chemical exchange among inequivalent sites can be excluded since only one such site is apparent in the spectra.

**$^{27}\text{Al}$ – $^{19}\text{F}$  Separated-Local-Field (SLF) 2D MAS NMR Experiments:** The relatively small nature and overall complexity underlying the thermal changes shown by the 1D  $^{27}\text{Al}$  and

(35) Dirken, P. J.; Jansen, J. B. H.; Schuiling, R. D. *Am. Mineral.* **1992**, *77*, 718.

(36) Rothwell, W. P.; Waugh, J. S. *J. Chem. Phys.* **1981**, *74*, 2721.

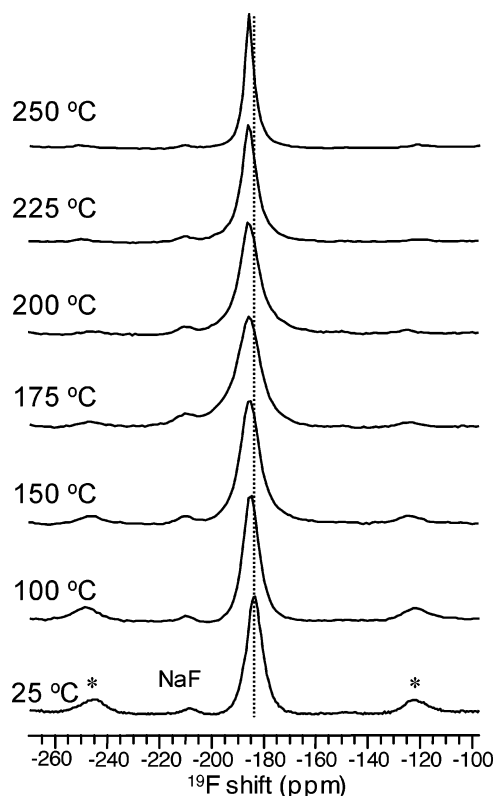


**Figure 11.** Variable temperature  $^{19}\text{F}$  MAS NMR spectra of cryolite acquired at a spinning speed of 20 kHz. Spinning sidebands (“\*”) and a NaF impurity are marked on the room-temperature spectrum.

$^{19}\text{F}$  MAS spectra between room temperature and 250 °C, prevent an assessment of the presumed  $\text{AlF}_6$  motions that originate them. In consequence we decided to further refine these dynamic solid-state NMR measurements, by monitoring the effective strength displayed by the Al–F dipolar couplings as a function of temperature. According to single-crystal data<sup>37</sup> the Al–F dipolar coupling characterizing cryolite’s octahedral site is  $\leq 5$  kHz, a fairly small number even in the absence of dynamics. To monitor the effective aluminum–fluorine dipolar couplings, amplified 2D separated local field (SLF) NMR experiments under the action of fast MAS (which is in turn desirable for the simple elimination of the homonuclear  $^{19}\text{F}$ – $^{19}\text{F}$  couplings) were recorded.<sup>38,39</sup> In such SLF MAS experiments rotor-synchronized pulses were applied to achieve a net heteronuclear dipolar evolution with variable amplification factors  $\times N$  of the  $^{27}\text{Al}$ – $^{19}\text{F}$  interaction along the indirect domain ( $\times 2$  SLF,  $\times 4$  SLF, and  $\times 8$  SLF),<sup>40,41</sup> followed by observation of aluminum’s central-transition  $\{^{19}\text{F}\}$ -decoupled evolution along the direct domain.<sup>42,43</sup> Such measurements were carried out at a 10 kHz MAS spinning rate and repeated as a function of temperature.

Figure 12 shows representative experimental dipolar MAS sideband patterns retrieved from these 2D  $^{27}\text{Al}$  SLF NMR results, together with best-fit simulations aimed at quantifying

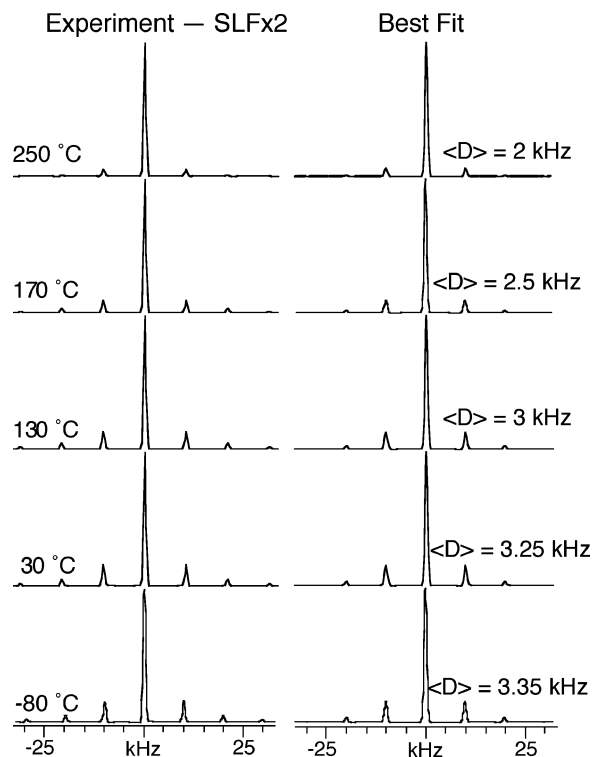


**Figure 12.** Illustration of representative 2D  $^{27}\text{Al}$ – $^{19}\text{F}$  amplified SLF experiments employed to retrieve the temperature dependence exhibited by the dipolar coupling between these nuclei. Experiments were carried out using the pulse sequences introduced in refs 42 and 43 under 10 kHz MAS; 2D  $^{27}\text{Al}$ -based spectra recorded as a function of temperature for amplification factors of 2, 4, and 8. All data were subsequently simulated as described in the text to obtain an average coupling as a function of temperature (Figure 13).

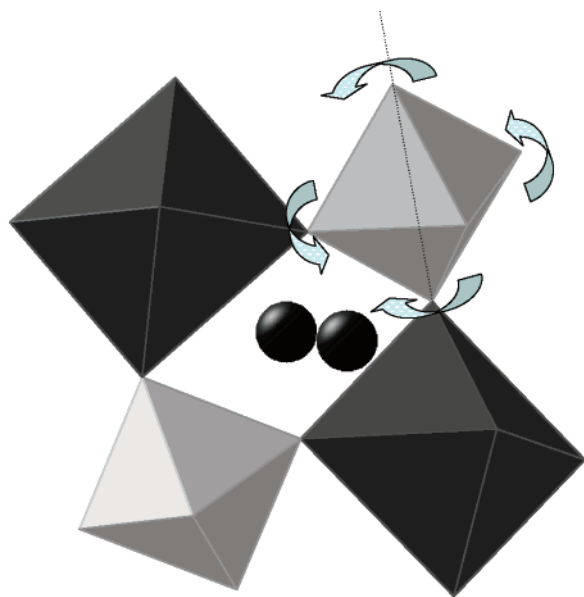
the average  $^{27}\text{Al}$ – $^{19}\text{F}$  dipolar couplings as a function of temperature. The experimental results confirm that, as temperature increases, the  $^{27}\text{Al}$ – $^{19}\text{F}$  average dipolar coupling is reduced. Assuming a model for this weakening in the coupling could enable one to extract further insight on the motion of the  $\text{AlF}_6$  octahedra. As usual, however, ambiguities arise from the fact that several different motional models can be assumed to successfully reproduce the thermal variations observed in the experimental NMR spectra. For the sake of simplicity we decided to adopt what is arguably the simplest of all dynamic models, consisting of a librational motion where all  $\text{AlF}_6$  rock within identical square-well potentials as rigid octahedral bodies (Scheme 1). Such a model was then used to estimate variations in the effective  $^{27}\text{Al}$ – $^{19}\text{F}$  dipolar tensor in terms of the averaging process

$$\bar{D}_{ij} = \int d\Omega P(\Omega) D_{ij}(\Omega) \quad (11)$$

where  $P(\Omega)$  denotes a square-well-type librational distribution, and the averaging assumes that the rocking motion occurs so fast that it only affords an exchange-averaged value. This model also employed as starting point a prototypical “static” Al–F dipolar coupling  $D_0 \approx 3.35$  kHz, which was the value extracted at  $-80$  °C from reference SLF data. Spin simulations were then carried out considering the central transition of the  $^{27}\text{Al}$  as a fictitious spin  $1/2$ , placing all six dipole-coupled neighboring  $^{19}\text{F}$  in a symmetric octahedron, and neglecting homonuclear  $^{19}\text{F}$ – $^{19}\text{F}$  couplings in view of the relatively fast MAS rates and short evolution times involved.<sup>42</sup> With the help of all these

- (37) Hawthorne, F. C.; Ferguson, R. B. *Can. Mineral.* **1975**, *13*, 377.  
 (38) Munowitz, M. G.; Griffin, R. G.; Bodenhausen G.; Wang T. H. *J. Am. Chem. Soc.* **1981**, *103*, 2529.  
 (39) Schaefer, J.; McKay, R. A.; Stejskal, E. O.; Dixon, W. T. *J. Magn. Reson.* **1983**, *52*, 123.  
 (40) Hong, M.; Gross, J. D.; Rienstra, C. M.; Griffin, R. G.; Kumashiro, K. K.; Schmidt-Rohr, K. *J. Magn. Reson.* **1997**, *129*, 85.  
 (41) McElheny, D.; DeVita, E.; Frydman, L. *J. Magn. Reson.* **2000**, *143*, 321.  
 (42) Grinshtein, J.; Grant, C. V.; Frydman, L. *J. Am. Chem. Soc.* **2002**, *124*, 13344.  
 (43) Grinshtein, J.; Frydman, L. *J. Am. Chem. Soc.* **2003**, *125*, 7451.

## Scheme 1



assumptions and relying on results from  $\times N$  SLF experimental data (Figure 13A), one can then estimate the average activation of an  $\text{AlF}_6$  octahedral libration as a function of temperature. These total libration angles (Figure 13B) indicate a marked increase in the local mobility above 120 °C, at a similar stage where the noticeable increase in line width was shown by the 1D  $^{19}\text{F}$  MAS traces and where extensive dynamics were revealed by the  $^{23}\text{Na}$  2D MAS exchange spectra.

## 5. Discussion

**A Solids NMR Perspective of Motions in Cryolite.** Our  $^{23}\text{Na}$  NMR experiments indicate that, whereas a marginal exchange happens between cryolite's Na1 and Na2 sites up to about 100 °C, this becomes fairly rapid and extensive at higher temperatures. Our results are qualitatively similar to those of Lacassagne et al.,<sup>20</sup> who estimated from 2D NMR a rate for the exchange between Na1 and Na2 at 200 °C of approximately  $353\text{ s}^{-1}$  for their (natural) cryolite sample. Spearing et al. obtained a rough estimate for the exchange rate at 100 °C of approximately 0.13 kHz for their synthetic cryolite, but no attempt to simulate the 1D spectra was made.<sup>18</sup> These authors also investigated a natural sample of cryolite, which showed considerably slower motions in the 120–130 °C temperature range as measured by the  $^{23}\text{Na}$  static line widths. A remarkable feature of the system that we analyzed was the large distribution in rates that could be measured for this exchange process. Distributions in rates might also have been present in samples investigated by other workers; however, it is difficult to estimate the size of these distributions unless careful simulations of the spectra are performed. We have previously observed large distributions in exchange rates in some materials containing small concentrations of defects that create vacancies or interstitials, with more rapid motion occurring nearby the defects.<sup>44,45</sup> Thus, we think it likely that our synthetic sample of cryolite also contained significant concentrations of defects. Cryolite per se does not contain any large vacancies in the structure; indeed, although oxidation-induced defects may be present in this

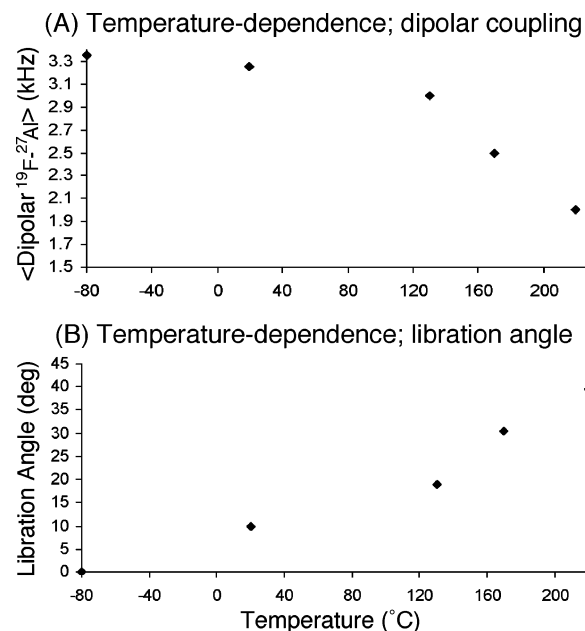


**Figure 13.** (A) Temperature dependence extracted for the average  $^{27}\text{Al}$ – $^{19}\text{F}$  dipolar couplings from 2D  $^{27}\text{Al}$ – $^{19}\text{F}$  SLF experiments of the kind illustrated in Figure 12. (B) Total libration angles calculated from the average dipolar couplings in (A), calculated with the help of a dynamic model whereby the  $\text{AlF}_6$  octahedron oscillates isotropically about its vertices.

synthetic sample, these are unlikely to produce Na vacancies unless such O-incorporation is associated with the presence of additional Al. Na1/Na2 exchange in a perfect lattice should therefore be associated with large activation barriers and probably involve a concerted process; consequently Na motion in the pure material is not expected to be significant at moderate temperatures. And yet, given the small NaF impurity evidenced by the  $^{19}\text{F}$  MAS NMR spectra, it is conceivable that our sample contained additional  $\text{Al}^{3+}$  dopants present on the Na1 site. Each  $\text{Al}^{3+}$  dopant would result in two  $\text{Na}^+$  vacancies, presumably on nearby Na2 sites, explaining the higher mobilities and the distribution in rates that we observe experimentally. This suggestion is consistent with the NaF– $\text{AlF}_3$  phase diagram, which shows that samples with the cryolite stoichiometry, prepared from the melt or quenched from elevated temperatures, will likely comprise a NaF-deficient cryolite plus a small amount of NaF.<sup>46,47</sup> Dewing has argued that the NaF deficiency in cryolite is accommodated by the formation of  $\text{AlF}_4^-$  ions, and of two further  $\text{Na}^+$  vacancies per  $\text{AlF}_4^-$  ion.<sup>47</sup> This mechanism would also account for the higher  $\text{Na}^+$  conductivity seen in our material, in comparison to that of the natural sample. We have seen no evidence for the  $\text{AlF}_4^-$  ion in the  $^{27}\text{Al}$  and  $^{19}\text{F}$  NMR spectra suggesting that this is not the major defect-formation mechanism, but we cannot exclude the possibility that this ion is present in very low concentrations.

Our  $^{19}\text{F}$  MAS NMR spectra reveal a broadening of the MAS line widths at approximately 200 °C, followed by a decrease in line width and significant sideband attenuation by 250 °C. Prior static  $^{19}\text{F}$  NMR work by Spearing et al. on a synthetic cryolite also revealed a dramatic narrowing of the static line shape above 100 °C, in comparison to the room-temperature line width (60

(44) Wang, F.; Grey, C. P. *Chem. Mater.* **1997**, *9*, 1068–1070.

(45) Wang, F.; Grey, C. P. *J. Am. Chem. Soc.* **1998**, *120*, 970–980.

(46) Solheim, A.; Sterten, A. Proc. 9th International Symposium on Light Metals Production, Tromø - Trondheim, Norway, Aug. 18th–21th, 1997; pp 225–234.

(47) Dewing, E. W. *Metal. Mater. Trans.* **1997**, *28B*, 1299.

kHz).<sup>18</sup> Lacassagne et al. used a slow MAS speed of 5 kHz to investigate their natural sample of cryolite.<sup>20</sup> They observed a broad line shape (spreading over 75 kHz) at room temperature, as well as two features within the line shape which were ascribed to different crystallographic sites. Consistent with our study and with that of Spearing et al.,<sup>18</sup> a collapse of the broad line shape was observed above 150 °C, and at 300 °C only a sharp resonance with weak sidebands remained. Based on our fast MAS spectra, it is clear that all the different fluoride-ion crystallographic sites in cryolite give rise to resonances with very similar chemical shifts, and thus the features seen in these slow MAS and static <sup>19</sup>F NMR experiments probably arose from a combination of the dipolar and shielding anisotropies, and not from different crystallographic sites. Yet all the <sup>19</sup>F NMR studies provide strong evidence for an AlF<sub>6</sub><sup>3-</sup> motion that by 300 °C involves a nearly isotropic rotation of the units, at least within the time scale probed by the <sup>19</sup>F MAS NMR experiments.

Our <sup>27</sup>Al 2D SLF experiments also indicate a rapid onset of the AlF<sub>6</sub> rocking motions above 120 °C. Within the constraints of the SLF experiment and of the rocking octahedron model assumed (Scheme 1), AlF<sub>6</sub> units appear to be executing fairly large amplitude motions already at 250 °C. The SLF <sup>27</sup>Al–<sup>19</sup>F data reveal that these motions are not yet isotropic at this temperature as residual <sup>27</sup>Al–<sup>19</sup>F dipolar coupling remains; yet the extent of the libration is definitely consistent with the <sup>19</sup>F MAS NMR behavior. Unfortunately, the inherent limitations of the 1D <sup>19</sup>F MAS and the 2D <sup>27</sup>Al SLF experiments prevent us from quantifying further details of this AlF<sub>6</sub><sup>3-</sup> dynamics, including the exchange rates involved and their distribution over the sample. Still, it is worth remarking that the onset of the AlF<sub>6</sub><sup>3-</sup> motion occurs within the same range as the onset of sodium exchange, and that the extent of AlF<sub>6</sub><sup>3-</sup> libration and the average Na exchange rate increase together as temperature is raised. Furthermore, the rapid spread in the distribution of <sup>23</sup>Na exchange rates that occurs in this temperature regime suggests that both a defect (e.g., a vacancy) and the presence of AlF<sub>6</sub><sup>3-</sup> motion are required for increasing the Na<sup>+</sup> mobility in this temperature range. All of this suggests that the two motions detected by the various dynamic solids NMR methods employed in this study, one concerning the AlF<sub>6</sub><sup>3-</sup> octahedra and the other an exchange between sodium sites, are actually correlated.

**Molecular Dynamic Simulations.** To get further insight into the meaning of these NMR results, a series of comparisons were made with molecular dynamics (MD) simulations carried out for cryolite and related systems.<sup>44,49,50</sup> Such MD simulations suggest that, for a defect-free system possessing a B(Na,Al)F<sub>6</sub> framework, three types of motions will be present: (1) At low temperature, the motion involves a rocking of the tilted corner-shared octahedra about the Al–Na interatomic vectors. (This motion has also been revealed by MD simulations for AlF<sub>3</sub>,<sup>50</sup> which is known to adopt a related ReO<sub>3</sub> structure where the A sites in the perovskite structure are empty and the B site is occupied by Al). The AlF<sub>6</sub> octahedra remain tilted at room temperature and the rocking of these octahedra does not affect

the tilt direction, the system maintaining a distortion from cubic symmetry to monoclinic and  $R\bar{3}c$  symmetry for Na<sub>3</sub>AlF<sub>6</sub> and AlF<sub>3</sub>, respectively.<sup>48,50</sup> Slow reorientational motion of the AlF<sub>6</sub> units occurs in this range for cryolite, within the time scale of the MD simulations. (2) More recent MD simulations suggest that at intermediate temperatures a motion involving a switch between the tilt directions of the BF<sub>6</sub> octahedra can occur.<sup>49</sup> (3) At higher temperatures, rapid, complete reorientations of the AlF<sub>6</sub> octahedra take place. The phase now appears cubic on average, although a snapshot of the structure would reveal bent Al–F–Na bonds. (The latter motion is not observed in AlF<sub>3</sub>, since there are no weak B–F bonds. In this system, the phase transition to a cubic structure occurs due to complete, 360° rotation about the Al–Al internuclear vector.<sup>50</sup>) The isotropic rotation of the AlF<sub>6</sub> groups in cryolite results in an increase in the volume available for Na<sub>2</sub> in the cavities, and thereby in a rapid increase in the Na<sub>1</sub>–Na<sub>2</sub> exchange rate at the onset of this motion.

Since our material remained monoclinically distorted throughout the explored temperature range, our experiments should only probe the first two of these motional regimes. Experiments are then in qualitative agreement with the MD calculations at ambient temperatures and allow for a quantification of the average Al–F librational angle, which is found to increase with temperature. Upon making a detailed comparison with the MD simulations, however, it is important to remark that due to their inherent nature SLF experiments are more sensitive to the extent than to the time scale or microscopic details of the motion. At this point, therefore, it is difficult to pinpoint to what extent are fast librational motions of the AlF<sub>6</sub><sup>3-</sup> octahedron vis-à-vis slower reorientations and/or switchings of octahedral tilt direction<sup>49</sup> responsible for the experimental changes observed by <sup>27</sup>Al NMR, particularly when considering the <sup>19</sup>F MAS data presented here and in earlier studies,<sup>18,20</sup> which confirm that slow AlF<sub>6</sub><sup>3-</sup> reorientational motions do occur in this regime. The Na exchange, which is seen experimentally but not predicted in this temperature regime by the MD simulations, is probably reflecting the presence of defects in our synthetic cryolite samples. The presence of such defects may also affect the extent of AlF<sub>6</sub><sup>3-</sup> librations; all of this highlights the care that should be exercised upon comparing simulations for ideal materials with experimental results from real samples.

## 6. Conclusion

The study of dynamics is clearly one of the important research avenues opened up by methodological developments in half-integer, solid-state quadrupolar NMR. In this paper we have focused on 1D MAS and 2D MQMAS dynamic spectra, simulated with the help of a semiclassical McConnell–Bloch exchange formalism. It stems from these investigations that MQMAS NMR experiments can often be more sensitive to dynamics than MAS investigations owing to their anisotropic-echoing characteristics. This background was then used to study the behavior of synthetic cryolite, which is complex and not easily amenable to understanding from a single set of spectroscopic measurements. Experimental 1D MAS, 2D exchange, and 2D MQMAS <sup>23</sup>Na dynamic spectra were then recorded and analyzed and compared with ancillary <sup>19</sup>F MAS and <sup>27</sup>Al–<sup>19</sup>F 2D SLF dipolar coupling measurements performed at different temperatures. The NMR results suggest that synthetic cryolite is NaF deficient. This will result in the presence of Na<sup>+</sup>

(48) Castiglione, M. PhD Thesis, University of Oxford, 2001; Castiglione, M.; Chaudhuri, S.; Madden, P. M., unpublished.

(49) Foy, L. Part II Thesis, University of Oxford, 2004.

(50) Chaudhuri, S.; Chupas, P.; Wilson, M.; Madden, P. A.; Grey, C. P. *J. Phys. Chem. B* **2004**, *108*, 3437.



vacancies in the lattice, possibly caused by additional Al substitution on the B site to form the nonstoichiometric cryolite ( $\text{Na}_{2-2x}(\text{Al}_{1+x}\text{Na}_{1-x})\text{F}_6$ ). From all these results a picture emerged whereby it is the onset of  $\text{AlF}_6^{3-}$  octahedral librations, aided by the  $\text{Na}^+$  vacancies, which are responsible for the migration of sodium atoms among the different lattice sites and for the ensuing complex dynamics observed in the solid upon heating the mineral above room temperature.

**Acknowledgment.** We are thankful to Lin-Shu Du, Rob Schurko, Adonis Lupulescu, Julia Grinshtein, Mattias Eden, and

Paul Madden for useful discussions. This research was supported by a Philip M. Klutznick Fund for Research (Weizmann Institute) and by the Israeli Science Foundation (Grant No. 296/01). C.P.G. thanks the U.S. DOE for its support via Grant No. DEFG0296ER14681. M.K. is thankful to the Department of Higher Education, M. P. State Govt., India, for providing a sabbatical leave.

JA0549749